



**HAL**  
open science

## Buckling modes in pantographic lattices

Ivan Giorgio, Alessandro Della Corte, Francesco Dell 'Isola, David J. Steigmann

► **To cite this version:**

Ivan Giorgio, Alessandro Della Corte, Francesco Dell 'Isola, David J. Steigmann. Buckling modes in pantographic lattices. *Comptes Rendus Mécanique*, 2016, 344, pp.487-501. 10.1016/j.crme.2016.02.009 . hal-01294032

**HAL Id: hal-01294032**

**<https://hal.science/hal-01294032>**

Submitted on 26 Mar 2016

**HAL** is a multi-disciplinary open access archive for the deposit and dissemination of scientific research documents, whether they are published or not. The documents may come from teaching and research institutions in France or abroad, or from public or private research centers.

L'archive ouverte pluridisciplinaire **HAL**, est destinée au dépôt et à la diffusion de documents scientifiques de niveau recherche, publiés ou non, émanant des établissements d'enseignement et de recherche français ou étrangers, des laboratoires publics ou privés.

# Buckling modes in pantographic lattices

Ivan Giorgio <sup>a,d</sup>, Alessandro Della Corte <sup>b,d</sup> Francesco dell'Isola <sup>a,d</sup>,  
David J. Steigmann <sup>c,d</sup>,

<sup>a</sup>*Dipartimento di Ingegneria Strutturale e Geotecnica, Università di Roma La Sapienza, 00184 Roma, Italy*

<sup>b</sup>*Dipartimento di Meccanica e Aeronautica, Università di Roma La Sapienza, 00184 Roma, Italy*

<sup>c</sup>*Department of Mechanical Engineering, University of California - Berkeley, CA. 94720 USA*

<sup>d</sup>*International Research Center for the Mathematics and Mechanics of Complex Systems, Università dell'Aquila, Italy*

Received \*\*\*\*\*, accepted after revision ++++++

Presented by xxxxx

---

## Abstract

We study buckling patterns in pantographic sheets, regarded as two-dimensional continua consisting of lattices of continuously distributed fibers. The fibers are modelled as beams endowed with elastic resistance to stretching, shearing, bending and twist. Included in the theory is a non-standard elasticity due to geodesic bending of the fibers relative to the lattice surface. *To cite this article: A. Name1, A. Name2, C. R. Mecanique 333 (2005).*

## Résumé

**Modes de flambage dans des structures de type pantographique.** Nous étudions le flambage de milieux continus bidimensionnels. Ces milieux que nous appelons “feuilles pantographiques”, sont constitués par un réseau formé de deux familles orthogonales de fibres parallèles. Ces fibres sont considérées comme des poutres élastiques reliées entre elles à chaque intersection par une liaison pivot. Le modèle bidimensionnel continu utilisé généralise celui des plaques puisqu'il prend en compte l'énergie élastique liée à la courbure des fibres dans le plan de la structure.

*Pour citer cet article : A. Name1, A. Name2, C. R. Mecanique 333 (2005).*

*Key words:* Pantographic structures; Buckling; Second gradient models; Geodesic bending; Non-linear elasticity

*Mots-clés :* Structures pantographiques; Flambage; milieux continus du second gradient; flexion géodésique; Élasticité non linéaire

---

---

*Email addresses:* [ivan.giorgio@uniroma1.it](mailto:ivan.giorgio@uniroma1.it) (Ivan Giorgio), [alessandro.dellacorte.memocs@gmail.com](mailto:alessandro.dellacorte.memocs@gmail.com) (Alessandro Della Corte), [francesco.dellisola@uniroma1.it](mailto:francesco.dellisola@uniroma1.it) (Francesco dell'Isola), [dsteigmann@berkeley.edu](mailto:dsteigmann@berkeley.edu) (David J. Steigmann).

*Preprint submitted to Elsevier Science*

*February 5, 2016*

## 1. Introduction

We have recently developed a two-dimensional continuum theory of elastic surfaces [1] to describe the deformations of pantographic lattices. The lattices are composed of intersecting fibers, or rods, that form two orthogonal curvilinear families in a reference plane. Every material point of the continuum is a point of intersection of two fibers — one from each family. In a general three-dimensional deformation of the sheet, the convected fibers of the pantograph flex to conform to the evolving surface in three-space. This is modelled by assigning strain energy to the normal curvatures and twists of the fibers. In contrast to conventional plate theories, the present model also accounts for the geodesic bending of the fibers. This mode of deformation occurs when, for example, the lattice is bent while deforming in a fixed plane. In the continuum theory, geodesic bending manifests itself as a strain-gradient effect. The lattice substructure thus confers strain-gradient elasticity to the continuum [2–10]. Strain gradient models, and in general higher gradient ones, are today a very topical research subject, and many relevant results are available in both theoretical [11–13] and applicative [14–21] directions. These models naturally arise as homogenized limits of microstructured plates (see e.g. [22–28]).

A simpler version of the theory was used in [32] to model deformations of a lattice of initially straight rods in which the shear strain segregates into coexistent phases separated by narrow transition layers in which geodesic bending predominates. The present study extends and generalizes the results of [32], by using the framework outlined in [1]. Specifically, we consider herein fibers which are not straight lines in the reference configuration (sinusoids, and logarithmic spirals). The interest in these geometries lies in their peculiar mechanical effects, induced by arch-like response to external stresses and other effects already mentioned in the literature (see below, Section 3). Moreover, we performed here a numerical study that exhibits interesting and heretofore unknown two- and three-dimensional buckling patterns in presence of both rectilinear and curvilinear fibers. In Section 2, we recall the basic kinematics of the model, following [1]. In Section 4, we specify the basic constitutive structure in terms of a strain-energy function, measured per unit area of the initial plane. This is applied to initially curved lattices conforming to two types of coordinate systems: logarithmic spirals and sinusoidal coordinates. The relevant details are outlined in Section 5.

## 2. Kinematics of pantographic lattices

We adopt the model developed in [1, 33], in which the pantographic sheet is regarded as an elastic surface endowed with suitable kinematic descriptors and an associated constitutive response in the form of an areal strain-energy density. The latter is assumed to depend on the stretches of the fibers and on their curvatures and twists. Further, as tangential stretch gradients appear in the constitutive equations for one-dimensional models of thin fibers that account for finite-thickness effects [34, 35], we also include a constitutive sensitivity to the tangential derivatives of the stretches. In addition, we incorporate a non-standard constitutive sensitivity to the cross derivatives of the fiber stretches; these record the variation in the stretch of a fiber family as the (initially) orthogonal family is traversed. This effect is discussed more fully in [32]. To make the paper reasonably self contained, we devote the remainder of the present section to a brief summary of the theory proposed in [1].

The deformation of the surface is described by a map  $\mathbf{r}(\mathbf{x}): \Omega \mapsto E^3$ , where  $\Omega \subset E^2$  is a connected plane region in the 2D Euclidean space  $E^2$  and  $E^3$  is Euclidean 3-space. Let  $\mathbf{L}, \mathbf{M} \in E^2$  be orthogonal families of unit vectors defining the fiber trajectories prior to deformation. The fiber stretches  $\{\lambda, \mu\}$  and fiber trajectories  $\{\mathbf{l}, \mathbf{m}\}$  induced by the deformation are

$$\lambda \mathbf{l} = (\nabla \mathbf{r}) \mathbf{L} \quad \text{and} \quad \mu \mathbf{m} = (\nabla \mathbf{r}) \mathbf{M}, \quad (1)$$

where  $\nabla(\cdot)$  is the (two-dimensional) gradient with respect to  $\mathbf{x}$ . Here  $\mathbf{l}$  and  $\mathbf{m}$  are unit vectors spanning the deformed tangent plane at the material point  $\mathbf{x} \in \Omega$ . We use them to define the fiber shear angle  $\gamma$  by

$$\sin \gamma = \mathbf{l} \cdot \mathbf{m}. \quad (2)$$

Because  $\{\mathbf{L}, \mathbf{M}\}$  is an orthonormal basis at any point of  $\Omega$ , we may use (1) to derive the representation

$$\nabla \mathbf{r} = \lambda \mathbf{l} \otimes \mathbf{L} + \mu \mathbf{m} \otimes \mathbf{M} \quad (3)$$

and thus obtain the Cauchy-Green deformation tensor,  $\mathbf{C} = (\nabla \mathbf{r})^t \nabla \mathbf{r}$ , in the form

$$\mathbf{C} = \lambda^2 \mathbf{L} \otimes \mathbf{L} + \mu^2 \mathbf{M} \otimes \mathbf{M} + \lambda \mu \sin \gamma (\mathbf{L} \otimes \mathbf{M} + \mathbf{M} \otimes \mathbf{L}). \quad (4)$$

Further, Eqs. (1) provide

$$J \mathbf{n} = (\nabla \mathbf{r}) \mathbf{L} \times (\nabla \mathbf{r}) \mathbf{M}, \quad (5)$$

where  $\mathbf{n}$  is the unit normal to the deformed surface, and

$$J = \lambda \mu |\cos \gamma| \quad (6)$$

is the local areal dilation induced by the deformation. Accordingly,

$$\mathbf{l} \times \mathbf{m} = |\cos \gamma| \mathbf{n}. \quad (7)$$

To describe the fiber curvatures and twist we require the second gradient  $\nabla \nabla \mathbf{r}$  of the deformation. This may be represented in the form [1]

$$\nabla \nabla \mathbf{r} = \mathbf{r}_{|\alpha\beta} \otimes \mathbf{e}^\alpha \otimes \mathbf{e}^\beta, \quad (8)$$

where

$$\mathbf{r}_{|\alpha\beta} = S_{\alpha\beta}^\lambda \mathbf{r}_{,\lambda} + b_{\alpha\beta} \mathbf{n}. \quad (9)$$

Here  $(\cdot)_{|\alpha\beta}$  is the second covariant derivative with respect to an arbitrary convected curvilinear coordinate system on the reference plane  $\Omega$ , the  $b_{\alpha\beta}$  are the coefficients of the second fundamental form (the covariant curvature tensor) of the deformed surface, and the  $S_{\alpha\beta}^\lambda$  are terms involving the strain and strain gradient. The rather complicated explicit expressions are [1]

$$\begin{aligned} S_{\alpha\beta}^\lambda \mathbf{r}_{,\lambda} = & (\lambda L_\alpha)_{|\beta} \mathbf{l} + (\lambda^2 \eta_l L_\alpha L_\beta + \lambda \mu \phi_l L_\alpha M_\beta) \mathbf{p} \\ & + (\mu M_\alpha)_{|\beta} \mathbf{m} + (\mu^2 \eta_m M_\alpha M_\beta + \lambda \mu \phi_m M_\alpha L_\beta) \mathbf{q}, \end{aligned} \quad (10)$$

and

$$b_{\alpha\beta} = K_L L_\alpha L_\beta + K_M M_\alpha M_\beta + T (L_\alpha M_\beta + M_\alpha L_\beta), \quad (11)$$

where  $\eta_l$  and  $\eta_m$  are the geodesic curvatures of the deformed fibers;  $\phi_l$  and  $\phi_m$  are the so-called Tchebychev curvatures;

$$\mathbf{p} = \mathbf{n} \times \mathbf{l} \quad \text{and} \quad \mathbf{q} = \mathbf{n} \times \mathbf{m} \quad (12)$$

define the orthogonal trajectories of the fibers on the deformed surface; and,

$$K_L = \lambda^2 \kappa_l, \quad K_M = \mu^2 \kappa_m \quad \text{and} \quad T = \lambda \mu \tau, \quad (13)$$

where  $\kappa_l$  and  $\kappa_m$  are the normal curvatures of the deformed fibers and  $\tau$  measures the twist of the deformed surface. These are non-zero if the deformation is such as to generate a curvature of the surface in three-space. Accordingly, they describe those parts of the fiber curvatures that can be attributed to surface flexure, whereas the geodesic curvatures represent the components of fiber curvatures in the tangent planes of the deformed surface. The latter arise from the surface strain and the strain gradient; the explicit expressions are [36]

$$J \eta_l = \text{div}[(\mu \sin \gamma) \mathbf{L} - \lambda \mathbf{M}] \quad \text{and} \quad J \eta_m = \text{div}[\mu \mathbf{L} - (\lambda \sin \gamma) \mathbf{M}], \quad (14)$$

where  $\text{div}$  is the divergence on  $\Omega$ , whereas the Tchebychev curvatures are given by [36]

$$J\phi_l = J\eta_m + \lambda \mathbf{M} \cdot \nabla(\sin \gamma) \quad \text{and} \quad J\phi_m = J\eta_l - \mu \mathbf{L} \cdot \nabla(\sin \gamma). \quad (15)$$

Later, we will have occasion to exploit the *fiber decomposition* [1]

$$\nabla \nabla \mathbf{r} = (L^\alpha L^\beta \mathbf{r}_{|\alpha\beta}) \otimes \mathbf{L} \otimes \mathbf{L} + (M^\alpha M^\beta \mathbf{r}_{|\alpha\beta}) \otimes \mathbf{M} \otimes \mathbf{M} + (L^\alpha M^\beta \mathbf{r}_{|\alpha\beta}) \otimes (\mathbf{L} \otimes \mathbf{M} + \mathbf{M} \otimes \mathbf{L}), \quad (16)$$

which follows from (8), with

$$\mathbf{e}^\alpha = L^\alpha \mathbf{L} + M^\alpha \mathbf{M}, \quad (17)$$

and from the symmetry of  $\mathbf{r}_{|\alpha\beta}$  with respect to interchange of the subscripts.

In the reference configuration, i.e., in the absence of deformation, we have  $\nabla \mathbf{r} = \mathbf{1}$ , the two-dimensional identity on  $\Omega$ . It follows that  $\nabla \nabla \mathbf{r}$  vanishes in this configuration and hence that  $S_{\alpha\beta}^\lambda$  and  $b_{\alpha\beta}$  also vanish. Moreover,  $\eta_l$  and  $\eta_m$  reduce to

$$\eta_L = -\text{div} \mathbf{M} \quad \text{and} \quad \eta_M = \text{div} \mathbf{L}, \quad (18)$$

respectively. These are the geodesic curvatures of the fibers on the reference plane. They account for the initial curvatures of the fibers, which are assumed to be initially untwisted. The Tchebychev curvatures  $\phi_l$  and  $\phi_m$  reduce, respectively, to  $\eta_M$  and  $\eta_L$  in the reference configuration. Because the  $S_{\alpha\beta}^\lambda$  and  $b_{\alpha\beta}$  are Galilean invariant [1] and vanish in the reference configuration, they furnish natural strain measures in the present theory. The vanishing of  $b_{\alpha\beta}$  in the reference configuration follows trivially from the fact that the latter is a region on a plane. We have proved that the  $S_{\alpha\beta}^\lambda$  also vanish there, but nevertheless pause to verify this directly—as a check on (10)—before proceeding.

In the reference configuration (10) reduces to

$$S_{\alpha\beta}^\lambda \mathbf{e}_\lambda = (L_{\alpha|\beta} - \eta_M M_\alpha M_\beta - \eta_L M_\alpha L_\beta) \mathbf{L} + (M_{\alpha|\beta} + \eta_L L_\alpha L_\beta + \eta_M L_\alpha M_\beta) \mathbf{M}. \quad (19)$$

Using  $\mathbf{1} = \mathbf{L} \otimes \mathbf{L} + \mathbf{M} \otimes \mathbf{M}$  we can write

$$\nabla \mathbf{L} = (\nabla \mathbf{L}) \mathbf{L} \otimes \mathbf{L} + (\nabla \mathbf{L}) \mathbf{M} \otimes \mathbf{M}, \quad (20)$$

and then conclude that

$$\text{div} \mathbf{L} = \text{tr}(\nabla \mathbf{L}) = \mathbf{L} \cdot (\nabla \mathbf{L}) \mathbf{L} + \mathbf{M} \cdot (\nabla \mathbf{L}) \mathbf{M}. \quad (21)$$

The first term on the right is  $(\nabla \mathbf{L})^t \mathbf{L} \cdot \mathbf{L}$ , in which  $(\nabla \mathbf{L})^t \mathbf{L} = \mathbf{0}$  because  $\mathbf{L}(\mathbf{x})$  is a unit-vector field. It then follows from (18)<sub>2</sub> that  $\eta_M = \mathbf{M} \cdot (\nabla \mathbf{L}) \mathbf{M}$ . In the same way, we use (18)<sub>2</sub> to prove that  $\eta_L = -\mathbf{L} \cdot (\nabla \mathbf{M}) \mathbf{L} = \mathbf{M} \cdot (\nabla \mathbf{L}) \mathbf{L}$ , where the second equality is a consequence of  $(\nabla \mathbf{L})^t \mathbf{M} = -(\nabla \mathbf{M})^t \mathbf{L}$ , which in turn follows by computing the gradient of  $\mathbf{L} \cdot \mathbf{M} (= 0)$ . These results yield

$$(\nabla \mathbf{L}) \mathbf{L} = [\mathbf{L} \cdot (\nabla \mathbf{L}) \mathbf{L}] \mathbf{L} + [\mathbf{M} \cdot (\nabla \mathbf{L}) \mathbf{L}] \mathbf{M} = \eta_L \mathbf{M} \quad (22)$$

and

$$(\nabla \mathbf{L}) \mathbf{M} = [\mathbf{L} \cdot (\nabla \mathbf{L}) \mathbf{M}] \mathbf{L} + [\mathbf{M} \cdot (\nabla \mathbf{L}) \mathbf{M}] \mathbf{M} = \eta_M \mathbf{M}, \quad (23)$$

yielding

$$\nabla \mathbf{L} = \eta_L \mathbf{M} \otimes \mathbf{L} + \eta_M \mathbf{M} \otimes \mathbf{M}, \quad (24)$$

and implying that the first parenthesis in (19) vanishes identically. The second parenthetical term is disposed of similarly, and our claim is proved. The present model differs from that presented in [32] in that  $\{\mathbf{L}, \mathbf{M}\}$  are allowed here to be functions on  $\Omega$ .

### 3. Lattice arrangement

To specify the distribution of curvilinear lattice fibers on the reference plane, we identify any particular fiber, with unit-tangent field  $\mathbf{M}$ , say, as the locus of points on which a scalar field  $\varphi(\mathbf{x})$  assumes a constant

value. The family of all such fibers is then obtain by varying the value of the constant. The unit-tangent fields of the fibers are given by

$$\mathbf{L}(\mathbf{x}) = \nabla\varphi/|\nabla\varphi| \quad \text{and} \quad \mathbf{M}(\mathbf{x}) = \mathbf{k} \times \mathbf{L}(\mathbf{x}), \quad (25)$$

where  $\mathbf{k}$  is the unit normal to the reference plane (i.e., the value of the surface-normal field  $\mathbf{n}$  in the reference configuration).

### 3.1. Technological applications for different geometries of the fibers

In the opinion of the authors, it has been proven by countless examples that byproducts of what looked like pure ‘amusement’ paid off extremely well in applications. More often than not, pursuing the aim of Jean Dieudonné, i.e. studying a subject only *pour l’honneur de l’esprit humain*, has been the best policy in order to concretely improve our lives. This mere consideration could serve as a justification for studying a certain scientific subject, as long as its theoretical foundation is clear and sound enough. However, in our specific case, direct reference to existing or conceivable application can be mentioned concerning particular geometries for the fibers.

In recent years, spiral woven fabrics are increasingly employed and examples of these artifacts can be found in many fields concerning e.g. biomedical, aerospace and automotive applications, including spinning components like flywheels or turbine blisks [29]; the reason behind the interest for spiral geometry lies in the possibility of combining circumferential fiber orientation for strength and radial fiber to manage interlaminar stresses [29]. However, theoretical coverage of this type of geometry for the fibers is still not very developed. This seems indeed one of the cases in which technological potential is being exploited even before a fully comprehensive understanding is reached.

Sinusoidal fibers furnish continuous-curvature approximations to the curved lattices adopted in the design of flexible electronics for health-monitoring purposes [30, 31]. Such devices are applied to skin tissue and are conceived to stick perfectly on it, possibly exhibiting complex large-deformation behavior, including out-of-plane buckling. The aim of the following sections is to provide some insight in the possible behavior of the two relatively complex geometries before mentioned.

#### 3.1.1. Logarithmic spirals

These woven fabrics are associated with the orthogonal curvilinear coordinates

$$\varphi = \log(r/r_0) - k\theta \quad \text{and} \quad \psi = k\log(r/r_0) + \theta, \quad (26)$$

where  $r_0$  and  $k$  are fixed parameters and  $\{r, \theta\}$  are plane polar coordinates. We compute

$$\nabla\varphi = \frac{1}{r}(\mathbf{e}_r - k\mathbf{e}_\theta), \quad (27)$$

where  $\{\mathbf{e}_r, \mathbf{e}_\theta\}$  is the standard orthonormal basis associated with the polar coordinates. Thus,

$$\mathbf{L}(\mathbf{x}) = \frac{1}{\sqrt{1+k^2}}(\mathbf{e}_r - k\mathbf{e}_\theta) \quad \text{and} \quad \mathbf{M}(\mathbf{x}) = \frac{1}{\sqrt{1+k^2}}(\mathbf{e}_\theta + k\mathbf{e}_r). \quad (28)$$

This is expressed directly in terms of  $\mathbf{x}(=x_\alpha\mathbf{i}_\alpha)$  by substituting

$$r = |\mathbf{x}|, \quad \mathbf{e}_r = r^{-1}\mathbf{x} \quad \text{and} \quad \mathbf{e}_\theta = \mathbf{k} \times \mathbf{e}_r. \quad (29)$$

#### 3.1.2. Oscillatory lattice

The fiber net which we consider here is described by

$$x_2 = A \sin(\omega x_1) + \varphi, \quad (30)$$

in which the amplitude and frequency parameters  $A$  and  $\omega$  are taken to be fixed. This immediately determines  $\varphi(\mathbf{x})$ , and hence  $\mathbf{L}(\mathbf{x})$  and  $\mathbf{M}(\mathbf{x})$  via Eq. (25). We omit the details of the trivial calculation.

#### 4. Strain-energy function

All constitutive information is contained in an areal strain-energy density  $W$  that depends on the first and second gradients of the deformation. To non-dimensionalize the variables appearing in this function it is necessary to introduce a local length scale. This could be the thickness of the actual sheet, the characteristic spacing of the internal points of intersection of rods of the actual pantographic lattice, or the widths of the constituent fibers. If any of these is used as the length scale, and if the couple stresses and bending/twisting moments vanish when the lattice is undeformed, then in practice the non-dimensionalized second gradient of the deformation is sufficiently small as to justify a quadratic dependence in the strain-energy function. A simple strain-energy function of this type, incorporating the curvilinear orthotropic symmetry associated with the initial fiber geometry, is [32]

$$W = w(\epsilon_L, \epsilon_M, J) + \frac{1}{2}A_L |L^\alpha L^\beta \mathbf{r}_{|\alpha\beta}|^2 + \frac{1}{2}A_M |M^\alpha M^\beta \mathbf{r}_{|\alpha\beta}|^2 + \frac{1}{2}A_\Gamma |L^\alpha M^\beta \mathbf{r}_{|\alpha\beta}|^2, \quad (31)$$

where the coefficients  $A_{L,M,\Gamma}$  are constants; this form is assumed for the sake of definiteness and tractability. Other forms are, of course, possible. We take  $A_{L,M,\Gamma}$  and to be strictly positive and observe, from the fiber decomposition (16), that the part of the energy depending on the second gradient  $\nabla\nabla\mathbf{r}$  is then non-negative, vanishing if and only if all  $\mathbf{r}_{|\alpha\beta}$  vanish simultaneously. It is thus a convex function of  $\nabla\nabla\mathbf{r}$ , ensuring the existence of energy-minimizing deformations in conservative boundary-value problems [37]. Further, the existence of a solution to the weak form of the equilibrium equations for similar problems in second-gradient elasticity has been proved in [38], albeit under hypotheses slightly more stringent than those satisfied here.

The constitutive sensitivities to geodesic and normal curvatures may be understood in terms of the mechanics of the lattice substructure. Thus, fibers offer resistance to bending in three-space, which may be resolved into geodesic bending and surface flexure. Fiber twist is determined by the twist of the surface because of the presumed connectivity of the lattice; that is, both families of intersecting fibers are assumed to pivot about the normal to the deformed surface at their points of intersection. This constraint implies that fiber twist is controlled entirely by surface geometry and is therefore not an independent kinematic variable [1].

For the strain-dependent function  $w$ , we adopt

$$w(\epsilon_L, \epsilon_M, J) = \frac{1}{2}(E_L \epsilon_L^2 + E_M \epsilon_M^2) - G(\ln J + 1 - J), \quad (32)$$

where

$$\epsilon_L = \frac{1}{2}(\lambda^2 - 1), \quad \epsilon_M = \frac{1}{2}(\mu^2 - 1) \quad (33)$$

are the extensional fiber strains and  $E_{L,M}$  and  $G$  are positive constants. This energy does not include a term proportional to  $\epsilon_L \epsilon_M$  and therefore does not exhibit a Poisson effect with respect to the fiber axes. Poisson effects are typically negligible in pantographic lattices. Finally, the term involving  $J$  penalizes fiber collapse ( $J \rightarrow 0$ ) by imposing unbounded growth of the attendant energy, whereas the remaining terms are appropriate for small-to-moderate fiber strains.

Our solution procedure, discussed in Section 5, is a finite-element scheme based on the weak form of the equilibrium equations derived from the proposed strain-energy function. This is not presented here, but reference may be made to [1], where the weak and strong formulations are given explicitly. Recent

applications of the finite element method and related methods to second-gradient elasticity are discussed in [39–47].

We observe that in Eq. (31) the contravariant components  $L^\alpha$  and  $M^\alpha$ , and the covariant derivatives  $\mathbf{r}_{|\alpha\beta}$ , pertain to any convected coordinate system. Moreover, the symmetry  $\mathbf{r}_{|\alpha\beta} = \mathbf{r}_{|\beta\alpha}$  implies that the ordering in the final term of Eq. (31) is irrelevant; i.e.,  $L^\alpha M^\beta \mathbf{r}_{|\alpha\beta} = M^\alpha L^\beta \mathbf{r}_{|\alpha\beta}$ .

It would be natural to identify the coordinates with the fiber parameters  $\varphi$  and  $\psi$  of Section 3, but here, for the sake of tractability, we exploit the underlying coordinate invariance and instead choose them to be Cartesian on  $\Omega$ . In this case the distinction between co- and contra-variance disappears, covariant derivatives reduce to partial derivatives, and Eq. (31) becomes

$$W = w(\epsilon_L, \epsilon_M, J) + \frac{1}{2}A_L |L_\alpha L_\beta \mathbf{r}_{,\alpha\beta}|^2 + \frac{1}{2}A_M |M_\alpha M_\beta \mathbf{r}_{,\alpha\beta}|^2 + \frac{1}{2}A_\Gamma |L_\alpha M_\beta \mathbf{r}_{,\alpha\beta}|^2, \quad (34)$$

with

$$J = |L_\alpha M_\beta \mathbf{r}_{,\alpha} \times \mathbf{r}_{,\beta}|, \quad \epsilon_L = E_{\alpha\beta} L_\alpha L_\beta \quad \text{and} \quad \epsilon_M = E_{\alpha\beta} M_\alpha M_\beta, \quad (35)$$

where

$$E_{\alpha\beta} = \frac{1}{2}(\mathbf{r}_{,\alpha} \cdot \mathbf{r}_{,\beta} - \delta_{\alpha\beta}), \quad (36)$$

with  $\delta_{\alpha\beta}$  the Kronecker delta, is the strain. Here,  $\mathbf{r}_{,\alpha} = r_{i,\alpha} \mathbf{i}_i$ , with  $\mathbf{i}_3 = \mathbf{i}_1 \times \mathbf{i}_2$ ;  $\{\mathbf{i}_k\}$  a fixed orthonormal basis associated with the Cartesian coordinates, and  $\mathbf{r}_{,\alpha\beta} = r_{i,\alpha\beta} \mathbf{i}_i$ . In the examples considered, the Cartesian components  $L_\alpha(\mathbf{x})$  and  $M_\alpha(\mathbf{x})$  are easily read off from the formulas provided in Section 3.

## 5. Examples

Numerical simulations here shown are based on Finite Element Analysis and performed with *COMSOL Multiphysics*<sup>®</sup> in the framework of a weak formulation. Because of the nature of the energy (31), we employed triangular Argyris elements having  $C^1$  continuity [32]. The number of mesh elements is  $\approx 10^4$ , which considering the 21 degrees of freedom of each element, provide a total of  $\approx 10^5$  degrees of freedom.

In the performed simulations, we adopt the representation [1]:

$$L_\alpha L_\beta \mathbf{r}_{,\alpha\beta} = \mathbf{g}_l + K_L \mathbf{n}, \quad M_\alpha M_\beta \mathbf{r}_{,\alpha\beta} = \mathbf{g}_m + K_M \mathbf{n}, \quad L_\alpha M_\beta \mathbf{r}_{,\alpha\beta} = \mathbf{\Gamma} + T \mathbf{n} \quad (37)$$

where  $\mathbf{g}_{l,m}$  and  $\mathbf{\Gamma}$  account for geodesic bending in the tangent plane of the deformed surfaces and  $\mathbf{n}$  is the (varying) unit normal to the surface. The variables  $K_{L,M}$  and  $T$  are the normal curvatures of the embedded fibers and the twist induced by the bending of the surface in three-space. With this notation, in Eq. (31), the part of the energy depending on the second gradient  $\nabla \nabla \mathbf{r}$  can be decomposed into the three following contributions which allow to emphasize the role of each term: i) the strain-gradient energy,

$$W_{SGE} = \frac{1}{2}A_L |\mathbf{g}_l|^2 + \frac{1}{2}A_M |\mathbf{g}_m|^2 + \frac{1}{2}A_\Gamma |\mathbf{\Gamma}|^2; \quad (38)$$

ii) the normal bending energy,

$$W_{NBE} = \frac{1}{2}A_L K_L^2 + \frac{1}{2}A_M K_M^2; \quad (39)$$

and iii) the twisting energy,

$$W_{TE} = \frac{1}{2}A_\Gamma T^2. \quad (40)$$

Because the normal derivative of position is not assigned, implicitly we are assigning zero double force on edges where position is assigned. Elsewhere we assign zero double force and zero traction unless otherwise specified.

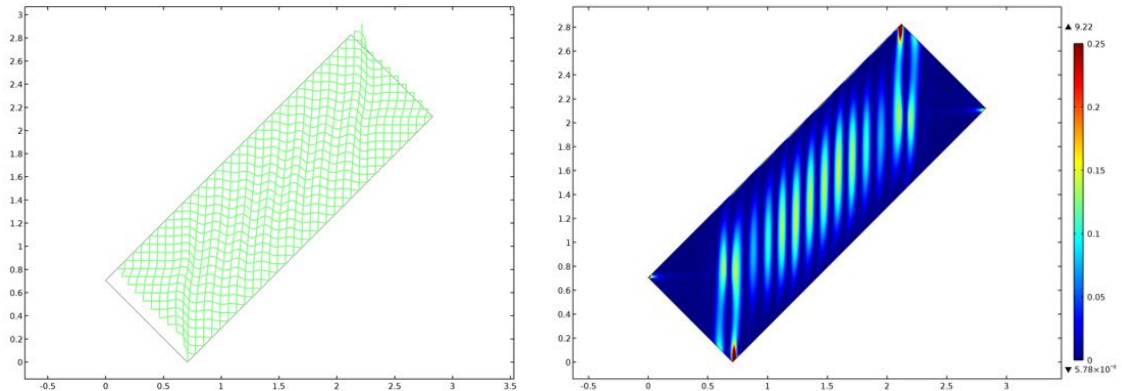


Figure 1. Geodesic buckling for the case of plane shear: fiber pattern (left) and the strain-gradient energy (right).

In the considered examples, a non-dimensional form of the problem is achieved by normalizing the strain energy with respect to a reference stiffness  $E_0$ , i.e.:

$$\tilde{W} = \frac{W}{E_0} \quad (41)$$

As a consequence of this normalization, the material parameters associated with Eq. (34) become:

$$\tilde{E}_L = \frac{E_L}{E_0}, \quad \tilde{E}_M = \frac{E_M}{E_0}, \quad \tilde{G} = \frac{G}{E_0}, \quad \tilde{A}_L = \frac{A_L}{E_0}, \quad \tilde{A}_M = \frac{A_M}{E_0}, \quad \tilde{A}_\Gamma = \frac{A_\Gamma}{E_0} \quad (42)$$

The lengths are normalized with respect to a reference length  $L_0$ , whose value will be specified case by case. In what follows, quantities in non-dimensional form are denoted with a superimposed tilde.

Herein we study the buckling mode shapes of the considered pantographic fibered structures. These two-dimensional continua are highly sensitive to geometrical and mechanical imperfections. Specifically, defects that may be encountered are: some differences in the directions of fiber pattern, delaminations or initial transverse deformations, variations in thickness, inclusions, eccentricity of loading and so forth. For numerical purposes, rather than perturbing the geometry, it is often easier to obtain the perturbation using an additional load or a further constraint on the displacement. This latter approach is the one followed in this paper. The heuristic method employed here for fibered pantographic sheets is sufficient for the immediate goal of determining some equilibrium shapes, but of course a rigorous analysis is needed in order to successfully predict buckling modes (see e.g. [48–52] for specific analytical tools concerning buckling and postbuckling).

### 5.1. Geodesic and out-of plane buckling of a lattice with initially straight fibers

In this section, we consider a rectangle plane region  $\Omega$  whose sides are in the ratio 1:3, with the longest of them being parallel to the bisector of the first quadrant of the reference plane. The two orthogonal families of fibers are arranged so as to form an angle of 45 degrees with the sides of this region; thus,  $\mathbf{L}, \mathbf{M}$  are constant unit vectors and coincide with the basis elements  $\mathbf{e}_1, \mathbf{e}_2$  associated with a Cartesian system. The shorter edge is used as the length scale for non-dimensionalization.

A first simulation is performed by imposing a shear displacement ( $\tilde{u}_0 = 0.1\sqrt{2}$ ) on one of the long sides and by fixing the opposite one, while the short sides are left free. The non-dimensional material parameters employed in this case are:  $\tilde{E}_L = \tilde{E}_M = 100$ ;  $\tilde{G} = 0.03$ ;  $\tilde{A}_\Gamma = 0.1$ ;  $\tilde{A}_L = \tilde{A}_M = 0.001$ . In this case to take imperfections into account, we impose on the displaced long side the additional constraint

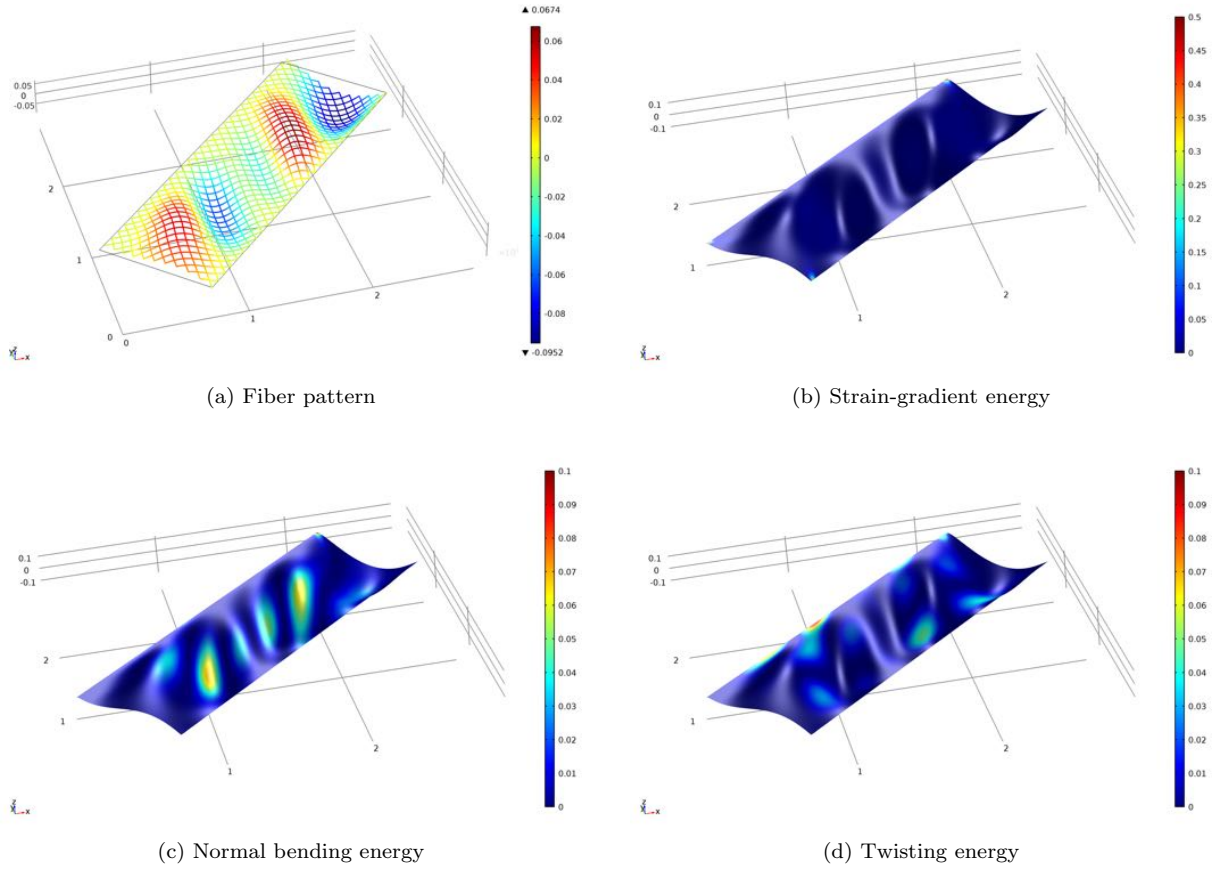


Figure 2. Case of initially straight fibers with compression ( $\tilde{v}_0 = 0.007\sqrt{2}$ ) and shear ( $\tilde{u}_0 = 0.05\sqrt{2}$ ) displacement imposed.

on the derivatives of the displacement lying on the plane of the pantographic sheet and, in particular we impose:

$$\tilde{u}_{\alpha,\beta}n_\beta = \varepsilon \quad \text{with } \alpha, \beta = \{1, 2\},$$

$\varepsilon$  being a positive quantity equal to  $2.22 \times 10^{-16}$ .

In Fig. 1 is shown an example of buckling occurred in the plane of the two-dimensional continuum considered, that we call “geodesic buckling” because it is related to the strain-gradient energy of Eq. (38) and therefore to the geodesic curvatures which appear in this term of the energy. In particular, on the left side of the figure the fiber pattern of the 2D continuous sheet is shown, while on the right side is plotted the strain-gradient energy (38) which, in this case, represents the only term in the second gradient energy, the contributions related to the normal bending and twisting being zero.

The curves which are visible in the deformed shape of the body are simply selected mono-dimensional sets of material points which, in the reference configuration, are parallel to the field lines relative to the fields  $\mathbf{L}$  and  $\mathbf{M}$ .

Figure 2 shows an example of out-of-plane buckling. In Fig. 2a the equilibrium shape is exhibited (colors indicate the out-of-plane component of displacement). In this case, in addition to a shear displacement ( $\tilde{u}_0 = 0.05\sqrt{2}$ ) we have also imposed a displacement of compression ( $\tilde{v}_0 = 0.007\sqrt{2}$ ) on the same long side and the constraint:  $\tilde{u}_{\alpha,\beta}n_\beta = 0$ , with  $\alpha, \beta = \{1, 2\}$ ; the other sides are subject to the same constraints

of the case previously considered. The non-dimensional material parameters used in this case are:  $\tilde{E}_L = \tilde{E}_M = 100$ ;  $\tilde{G} = 0.02$ ;  $\tilde{A}_\Gamma = 0.1$ ;  $\tilde{A}_L = \tilde{A}_M = 0.01$ . To simulate imperfections, we set the condition for the derivatives of the displacement out-of-plane as:

$$\tilde{u}_{3,\beta}n_\beta = 1 \times 10^{-4} \quad \text{with } \beta = \{1, 2\}.$$

In this simulation, we can see how the strain-gradient energy (Fig. 2b) is localized mainly near the corners of the rectangular fibered sheet, while the normal bending energy (Fig. 2c) and the twisting energy (Fig. 2d) have greater relevance.

In the next simulations, we consider two examples with different material parameters to investigate how they affect the solution. The simulations are performed by imposing a compressive displacement ( $\tilde{u}_0 = 0.07\sqrt{2}$ ) on one of the long sides, by fixing the opposite one and leaving the short sides free. In addition, on the moving long side we assign the constraint:  $\tilde{u}_{\alpha,\beta}n_\beta = 0$ , with  $\alpha, \beta = \{1, 2\}$ . The non-dimensional material parameters employed in these cases are:

**Case I.**  $\tilde{E}_L = \tilde{E}_M = 100$ ;  $\tilde{G} = 0.02$ ;  $\tilde{A}_\Gamma = 0.1$ ;  $\tilde{A}_L = \tilde{A}_M = 0.1$ ;

**Case II.**  $\tilde{E}_L = \tilde{E}_M = 100$ ;  $\tilde{G} = 0.02$ ;  $\tilde{A}_\Gamma = 0.1$ ;  $\tilde{A}_L = \tilde{A}_M = 0.01$ .

To take imperfections into account, we impose on the moved long side the additional constrain on the derivatives of the displacement lying on the plane of the pantographic sheet and, in particular, we impose:

$$\tilde{u}_{\alpha,\beta}n_\beta = 1 \times 10^{-4} \quad \text{with } \alpha, \beta = \{1, 2\}$$

Figures 3 and 4 show the out-of-plane buckling modes in the cases examined. Specifically, these figures give details of the particular fiber pattern assumed in the current configuration (Figs. 3a and 4a), and of the terms of the second gradient energy above mentioned (i.e., Eqs. (38), (39) and (40)). Also in these simulations, we can see how the strain-gradient energy (Figs. 3b and 4b) is localized mostly near the corners of the rectangular fibered sheet and is of the same level in both cases; in the second case, when  $\tilde{A}_L = \tilde{A}_M = 0.01$  are smaller than  $\tilde{A}_\Gamma = 0.1$  the twisting energy attains a maximum in the center very high if compared with the first case (Figs. 3d and 4d); on the contrary, the normal bending energy achieves its maximum level in the first case (Figs. 3c and 4c). As a result, the two buckling modes obtained are enough different given that the relative rigidities of the terms of the second gradient energy promote a type of deformation rather than the other one.

Figure 5 shows the plot of convergence of the total energy stored versus mesh refinement, i.e. the inverse of the mesh size  $h$  in the two cases before examined. Of course, the convergence analysis here shown is not to be intended in the sense of a convergence toward a known limit solution, as there is no chance of getting a close form solution as a benchmark even with the simplest possible boundary conditions and constitutive assumptions. However, the analysis just shown strongly supports the claim that the set of numerical solutions one has decreasing the mesh size is a subset of a Cauchy sequence, i.e. the difference between any two solutions can be made arbitrarily small if the largest mesh size between the two is small enough.

## 5.2. Buckling of logarithmic spirals

In this section, we consider an annular two-dimensional sheet with fibers forming logarithmic spirals (Fig. 6). This fibered sheet is deformed by fixing it at the outer boundary and imposing a displacement at the inner boundary corresponding to a counterclockwise rotation of 30 degrees and a radial opening of amplitude  $\tilde{u}_0 = 0.06$ . The radius of the inner circle is 0.05 and that of the outer boundary is 0.2. The logarithmic spirals in the initial configuration (see Fig. 6-left) are characterized by the parameter  $k = \tan(\pi/4)$  and  $\tilde{r}_0 = 0.1$  (see Eq. (26)). The non-dimensional material parameters utilized in this case

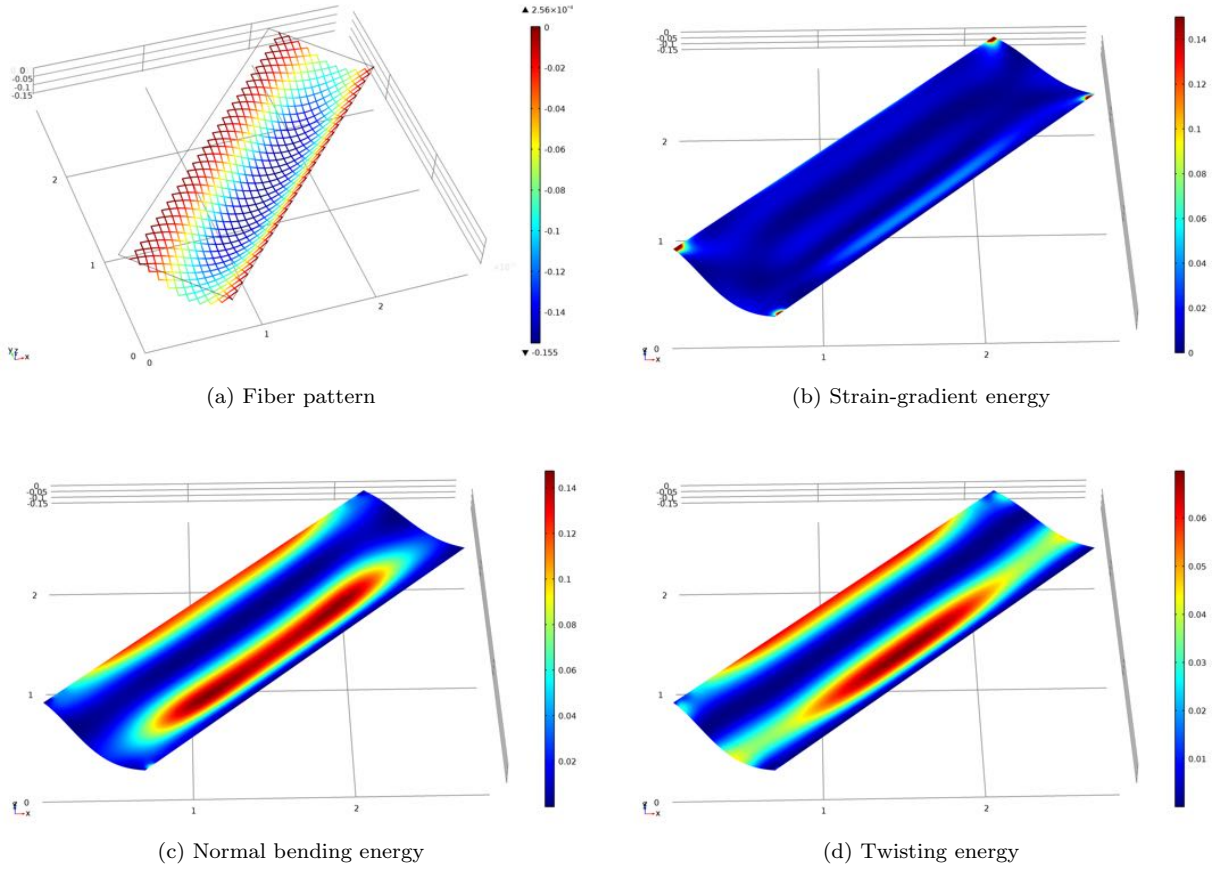


Figure 3. Case I ( $\tilde{A}_L = \tilde{A}_M = 0.1$ ): compressive displacement imposed ( $\tilde{u}_0 = 0.07\sqrt{2}$ ).

are:  $\tilde{E}_L = \tilde{E}_M = 500$ ;  $\tilde{G} = 0.1$ ;  $\tilde{A}_\Gamma = 0.1$ ;  $\tilde{A}_L = \tilde{A}_M = 0.01$ . Further, to simulate imperfections, we impose:

$$\begin{aligned} \tilde{u}_{3,\beta}\tilde{x}_\beta|\tilde{\mathbf{x}}|^{-1} &= 1 \times 10^{-3} && \text{with } \beta = \{1, 2\} \text{ on the outer boundary;} \\ \tilde{u}_{3,\beta}\tilde{x}_\beta|\tilde{\mathbf{x}}|^{-1} &= -1 \times 10^{-3} && \text{with } \beta = \{1, 2\} \text{ on the inner boundary.} \end{aligned}$$

Figure 7 shows the deformation shape of the annular fibered sheet, and in particular the pattern of fibers (Fig. 7a) —colors indicate the out-of-plane component of the displacement. Figure 7 shows also the three terms of the second gradient energy which in this case are significant.

### 5.3. Oscillatory lattice

In this case, we consider a rectangle plane region  $\Omega$  whose sides are in the ratio 0.75:1. The longer edge is used as the length scale for non-dimensionalization. The parameters characterizing the oscillatory fibers which appear in Eq.(30) are assumed to be  $\tilde{A} = A/L_0 = 0.25$ ,  $\tilde{\omega} = \omega L_0 = 4\pi$ .

In a first case, we examine the standard bias extension test in which one of the longer side is fixed and on the other edge a displacement  $\tilde{u}_0 = 0.2$  is imposed in the direction orthogonal to the same side. On the remaining edges, we assign zero double force and zero traction.

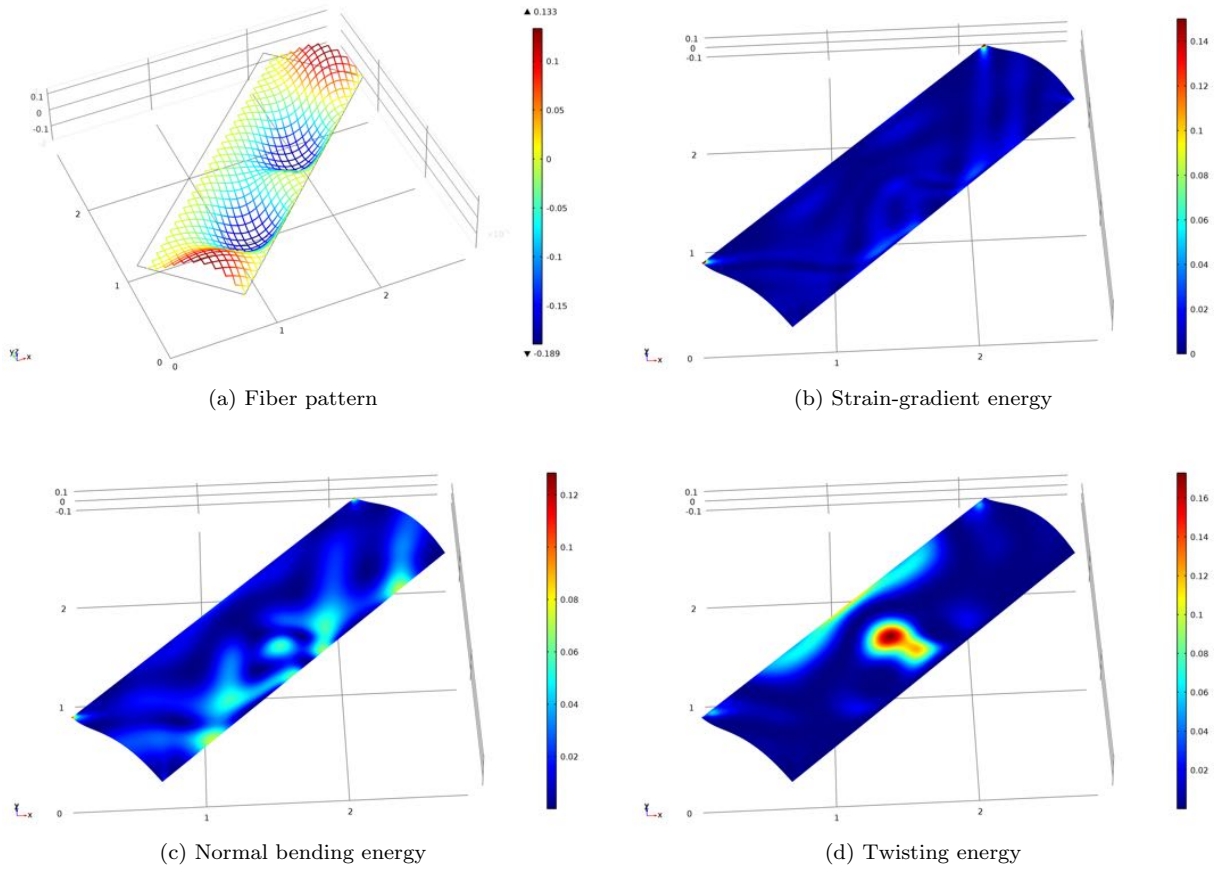


Figure 4. Case II ( $\tilde{A}_L = \tilde{A}_M = 0.01$ ): compressive displacement imposed ( $\tilde{u}_0 = 0.07\sqrt{2}$ ).

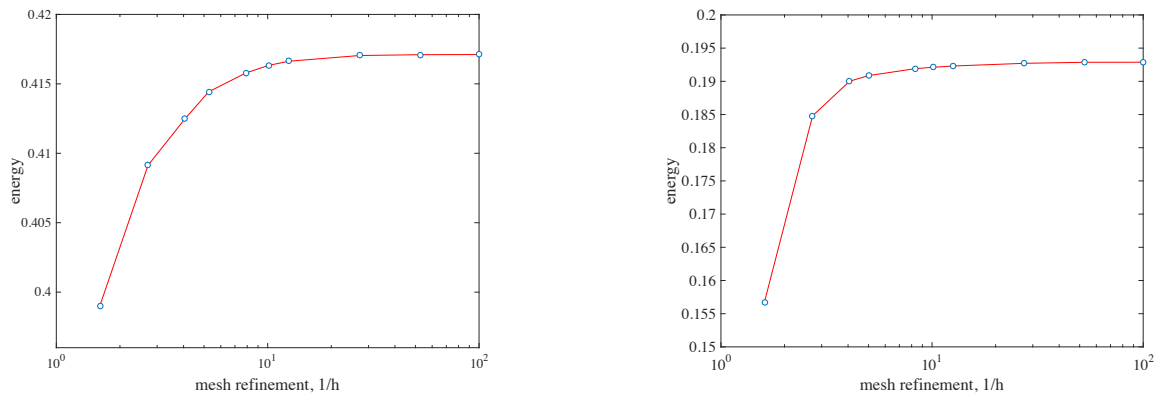


Figure 5. Convergence plots: Case I (left); Case II (right).

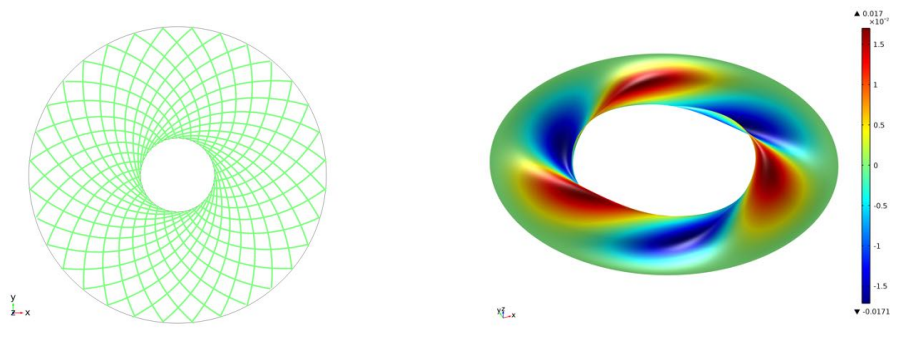


Figure 6. Buckling example with logarithmic spirals arrangement of fibers in the case of radial displacement ( $\tilde{u}_0 = 0.06$ ) and rotation (30 degrees) of the inner circle: Fiber pattern in the reference configuration (left); the shear strain relative to the initial fiber directions (right).

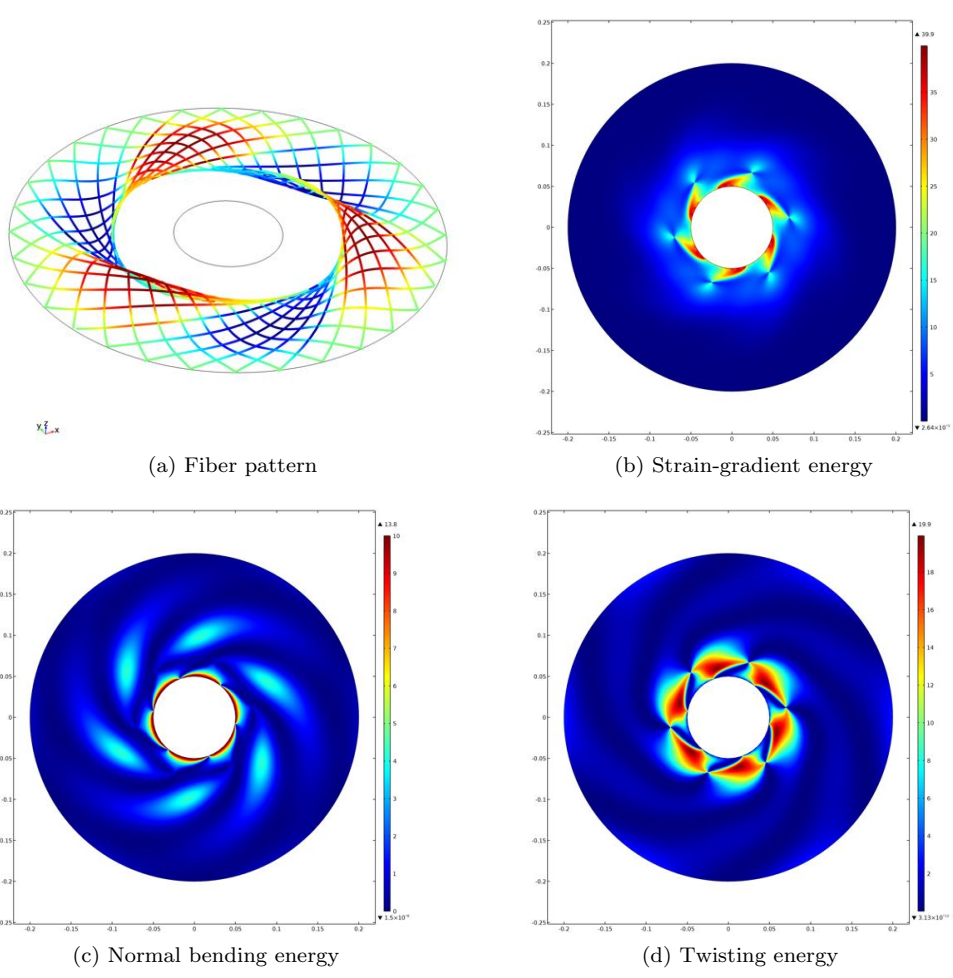


Figure 7. Buckling example with Logarithmic spirals arrangement of fibers: simulation with opening displacement ( $\tilde{u}_0 = 0.06$ ) and rotation (30 degrees) of the inner circle.

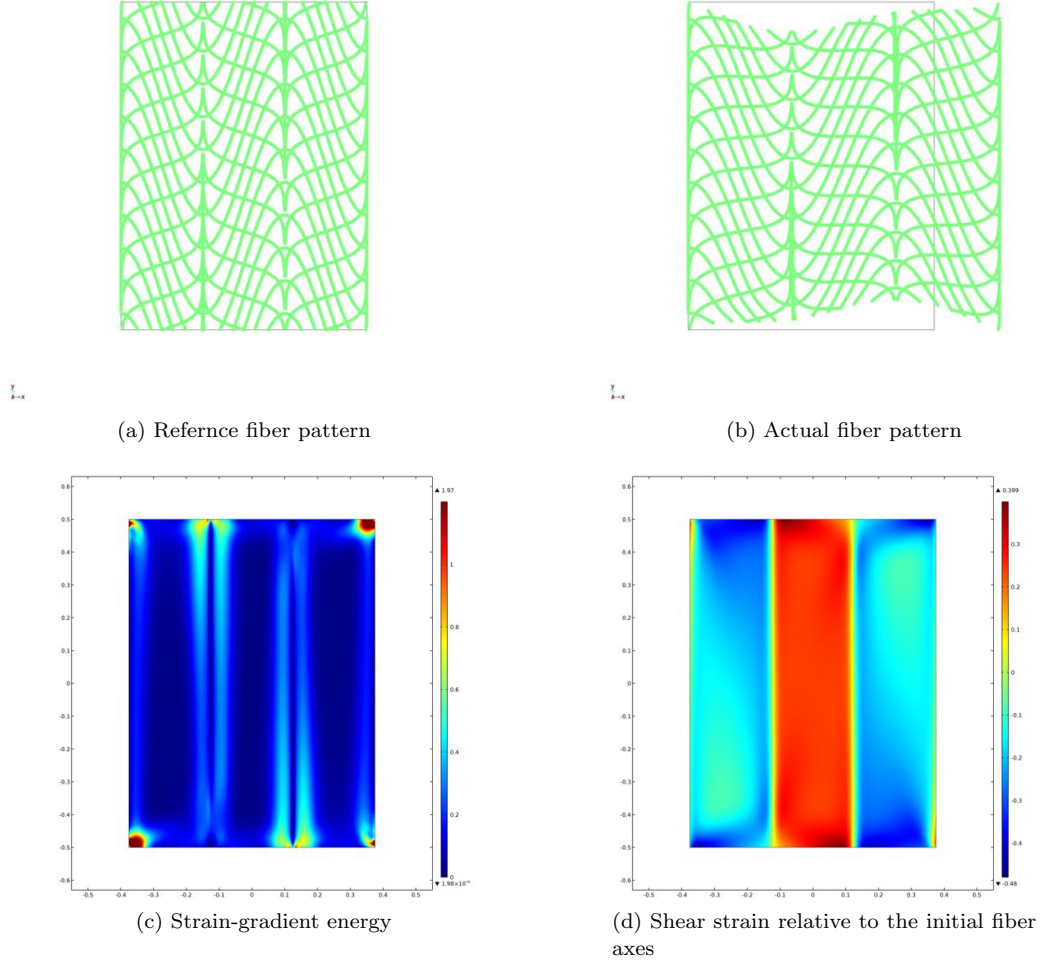


Figure 8. Bias extension test - displacement  $\tilde{u}_0 = 0.2$

Figure 8 displays the arrangement of the fibers in the reference configuration (Fig. 8a), the equilibrium shape of the sample after the deformation and the new disposition of the net (Fig. 8b), the second gradient energy (Fig. 8c) and the measure of the shear strain relative to the initial fiber axes (Fig. 8d). The more easily detectable feature in the plot of the shear strain (Fig. 8d) is the presence of three distinct bands in which the shear strain presents a distribution almost uniform.

In the next examples, we impose a shear displacement ( $\tilde{v}_0 = 0.2$ ) and a displacement of compression ( $\tilde{u}_0 = 0.2$ ) on one of the longer side being fixed the opposite one. We study two cases of buckling by assuming the following material parameters:

**Case a.**  $\tilde{E}_L = \tilde{E}_M = 100$ ;  $\tilde{G} = 0.2$ ;  $\tilde{A}_\Gamma = 0.1$ ;  $\tilde{A}_L = \tilde{A}_M = 0.01$ ;

**Case b.**  $\tilde{E}_L = \tilde{E}_M = 100$ ;  $\tilde{G} = 0.2$ ;  $\tilde{A}_\Gamma = 0.1$ ;  $\tilde{A}_L = \tilde{A}_M = 0.001$ .

To simulate imperfections, we impose on the moved long side the constraint:

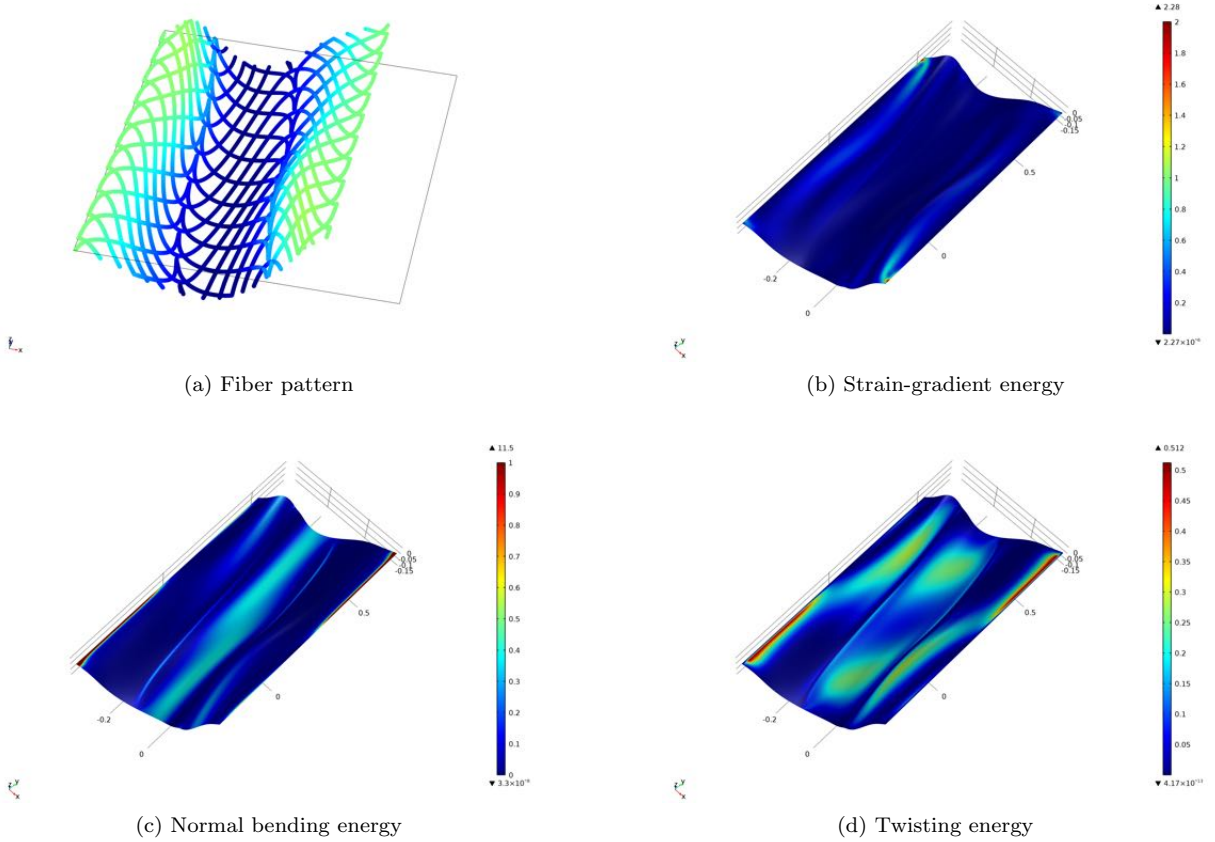


Figure 9. Case a: Compressive ( $\tilde{u}_0 = 0.2$ ) and shear ( $\tilde{v}_0 = 0.2$ ) displacement imposed ( $\tilde{A}_M = 0.01$ ).

$$\tilde{u}_{3,\beta}n_\beta = 1 \times 10^{-4} \quad \text{with } \alpha, \beta = \{1, 2\}$$

With this kind of application at hand, it is very interesting to investigate how changes in the constitutive parameters can affect the out-of-plane displacement of sinusoidal lattices. Indeed, epidermal electronics strongly requires a close to perfect adherence of the lattice to the skin surface, which means that a set of constitutive assumptions that robustly resist to buckling is to be preferred over a generic one. The simulations shown in Fig. 9 and 10 compare the case with  $\tilde{A}_M = 0.01$  and the one with  $\tilde{A}_M = 0.001$ . As one can see, in the latter case the average out-of-plane displacement is one order of magnitude smaller (0.0467 vs 0.00339), which means that a smaller second gradient stiffness  $\tilde{A}_M$  of the fibers may ensure a better adherence of the lattice to the skin surface. Specifically, these figures give details of the particular fiber pattern assumed in the current configuration—colors indicate the out-of-plane component of displacement—(Figs. 9a and 10a), and of the terms of the second gradient energy already considered, i.e. Eqs. (38), (39) and (40). Analogous considerations apply in these last cases as for the straight fibers regarding the second gradient terms of the energy considered.

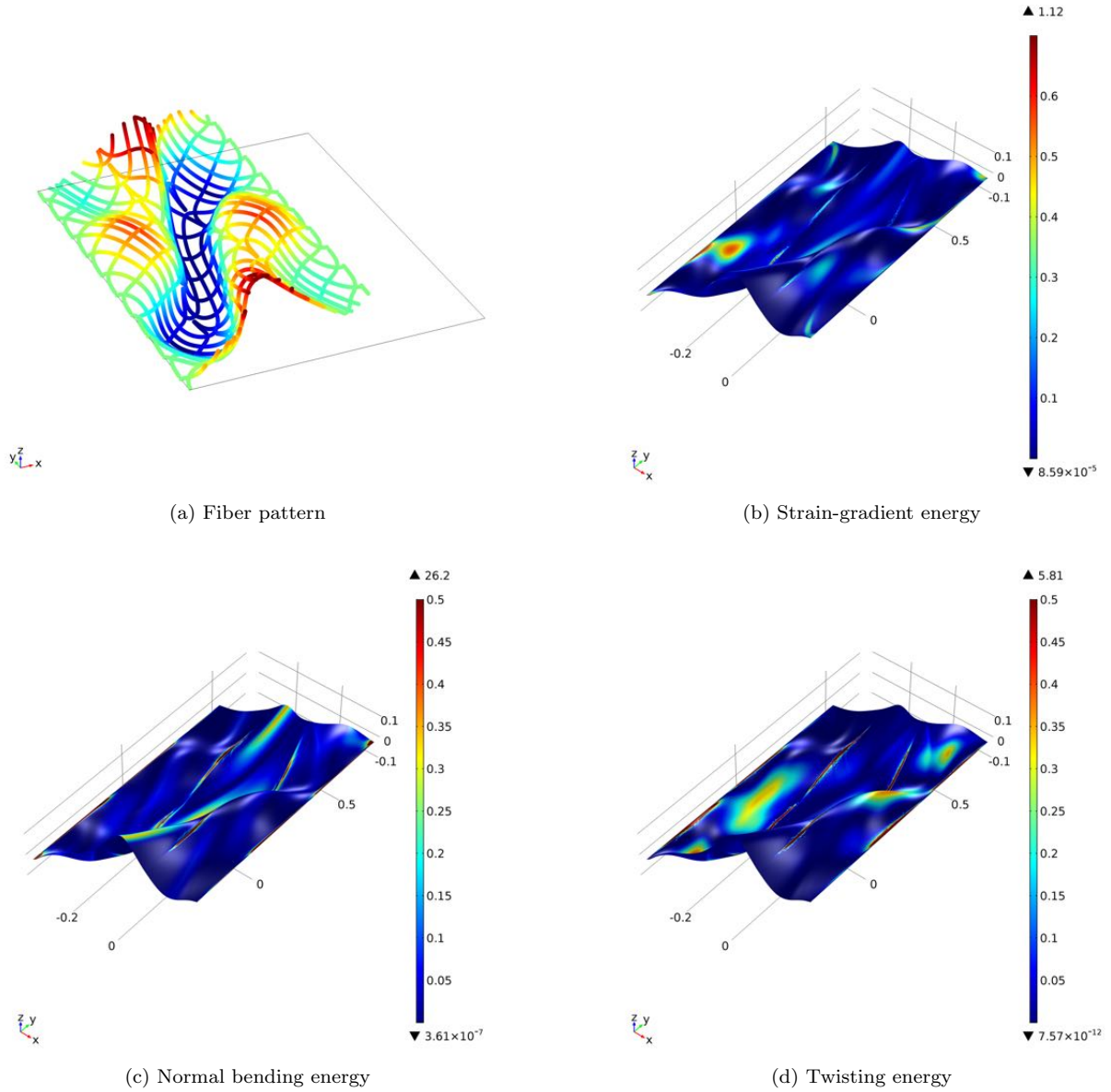


Figure 10. Case b: compressive ( $\tilde{u}_0 = 0.2$ ) and shear ( $\tilde{v}_0 = 0.2$ ) displacement imposed ( $\tilde{A}_M = 0.001$ ).

## 6. Conclusion

The numerical simulations performed on the basis of the theoretical model briefly described in Sections 2 and 4 provided some examples of mechanical instability. Specifically, out-of-plane buckling was observed with straight and curved fibres geometries. Moreover a more exotic in-plane buckling was also obtained in Fig. 1 concerning the simple case of straight orthogonal fibers. This buckling is linked to the fact that our continuum model is able to store energy in connection with the geodesic bending of the fibers,

which in turn is modeled by means of a strain gradient theory. The amount of energy stored in this way, when compared to the standard out-of-plane flexural and torsional energies, can be non-negligible, as demonstrated in simulations shown in Figs. 2,7, 9 and 10.

## Acknowledgements

The authors would like to thank Tomasz Lekszycki for his helpful comments and advice. The authors also thank the reviewer for having drawn their attention on the importance of explicitly showing connections between the object of their investigations and possible real-world applications.

## References

- [1] Steigmann DJ and dell’Isola F, Mechanical response of fabric sheets to three-dimensional bending, twisting, and stretching. *Acta Mech Sinica* 31 (2015) 373–382.
- [2] Toupin RA, Theories of elasticity with couple stress. *Arch. Rational Mech. Anal.* 17 (1964) 85–112.
- [3] Mindlin RD and Tiersten HF, Effects of couple-stresses in linear elasticity. *Arch. Rational Mech. Anal.* 11 (1962) 415–448.
- [4] Koiter WT, Couple-stresses in the theory of elasticity. *Proc. Kon. Ned. Akad. Wetensch.* B67 (1964) 17–44.
- [5] P. Germain P, The method of virtual power in continuum mechanics, part 2: microstructure. *SIAM J. Appl. Math.* 25 (1973) 556–575.
- [6] Grillo A, Federico S, Wittum G, Imatani S, Giaquinta G, Mićunović MV, Evolution of a fibre-reinforced growing mixture. *Il Nuovo cimento della Societ italiana di fisica. C* 32 (2009) 97–119.
- [7] Grillo A, Federico S and Wittum G, Growth, mass transfer, and remodeling in fiber-reinforced, multi-constituent materials. *Int. J. Non-Linear Mech.* 47 (2012) 388–401.
- [8] Forest S, Micromorphic approach for gradient elasticity, viscoplasticity and damage. *ASCE Journal of Engineering Mechanics* 135 (2009) 117–131.
- [9] Fosdick R, A generalized continuum theory with internal corner and surface contact interactions. *Contin. Mech. Thermodyn.* (2015) DOI: 10.1007/s00161-015-0423-8.
- [10] Camar-Eddine M, Seppecher P, Determination of the closure of the set of elasticity functionals. *Arch. Ration. Mech. Anal.* 170 (2003) 211–245.
- [11] dell’Isola F, Madeo A. and Seppecher P, Cauchy Tetrahedron Argument Applied to Higher Contact Interactions. *Arch. Rational Mech. Anal.* (2015) DOI: 10.1007/s00205-015-0922-6.
- [12] Pideri C, Seppecher P, A second gradient material resulting from the homogenization of an heterogeneous linear elastic medium. *Continuum Mech. Thermodyn.* 9 (1997) 241–257.
- [13] Placidi L, Andreaus U and Della Corte A, Gedanken experiments for the determination of two-dimensional linear second gradient elasticity coefficients. *Z. Angew. Math. Phys.* 66 (2015) 3699–3725.
- [14] dell’Isola F, Giorgio I and Andreaus U, Elastic pantographic 2D lattices: a numerical analysis on the static response and wave propagation. *Proc. Est. Acad. Sci. Eng.* 64 (2015) 219–225.
- [15] Madeo A, Neff P, Ghiba ID, Placidi L and Rosi G, Wave propagation in relaxed micromorphic continua: modeling metamaterials with frequency band-gaps. *Contin. Mech. Thermodyn.* 27 (2015) 551–570.
- [16] Rinaldi A, and Placidi L, A microscale second gradient approximation of the damage parameter of quasi-brittle heterogeneous lattices. *Z. angew. Math. Mech.* 94 (2014) 862–877.
- [17] Placidi L, A variational approach for a nonlinear one-dimensional damage-elasto-plastic second-gradient continuum model. *Contin. Mech. Thermodyn.* (2014) DOI: 10.1007/s00161-014-0405-2.

- [18] Placidi L, A variational approach for a nonlinear 1-dimensional second gradient continuum damage model. *Contin. Mech. Thermodyn.* 27 (2015) 623–638.
- [19] Yang Y, Ching, W, and Misra A, Higher-Order Continuum Theory Applied to Fracture Simulation of Nanoscale Intergranular Glassy Film. *J. Nanomech. Micromech.* 1 (2011) 60–71.
- [20] Del Vescovo D and Giorgio I, Dynamic problems for metamaterials: review of existing models and ideas for further research. *Internat. J. Engrg. Sci.* 80 (2014) 153–172.
- [21] dell’Isola F, Lekszycki T, Pawlikowski M, Grygoruk R and Greco L, Designing a light fabric metamaterial being highly macroscopically tough under directional extension: first experimental evidence. *Z. Angew. Math. Phys.* 66 (2015) 3473–3498.
- [22] Altenbach H, and Eremeyev VA, On the linear theory of micropolar plates. *Z. angew. Math. Mech.* 89 (2009) 242–256.
- [23] Altenbach H, Eremeyev VA, Lebedev LP and Rendón LA, Acceleration waves and ellipticity in thermoelastic micropolar media. *Arch. Appl. Mech.* 80 (2010) 217–227.
- [24] Altenbach H, and Eremeyev VA, Cosserat-type shells. Chapter in *Generalized Continua from the Theory to Engineering Applications* 541 of the series CISM (2013) 131–178.
- [25] Harrison P, Modelling the forming mechanics of engineering fabrics using a mutually constrained pantographic beam and membrane mesh. *Compos. Part A Appl. S.* 81 (2016) 145–157.
- [26] Eremeyev VA, Ivanova EA and Morozov NF, On free oscillations of an elastic solids with ordered arrays of nano-sized objects. *Contin. Mech. Thermodyn.* 27 (2015) 583–607.
- [27] Boubaker BB, Haussy B and Ganghoffer JF, Discrete models of woven structures. Macroscopic approach. *Compos Part B:Eng* 38 (2007) 498–505.
- [28] Dos Reis F and Ganghoffer JF, Equivalent mechanical properties of auxetic lattices from discrete homogenization. *Comput. Mater. Sci.* 51 (2012) 314–321.
- [29] Clarke SR, Net Shape Woven Fabrics–2D and 3D. *Journal of Industrial Textiles* 30 (2000) 15–25.
- [30] Kim DH, Lu N, Ma R, Kim YS, Kim RH, Wang S, Wu J, Won SM, Tao H, Islam A, and et al., Epidermal electronics. *Science* 333 (2011) 838–843.
- [31] dell’Isola F, Steigmann D and Della Corte A, Synthesis of complex structures. Designing micro-structure to deliver targeted macro-scale response. *Appl. Mech. Rev.* 67 (2016) 060804. DOI: 10.1115/1.4032206.
- [32] Giorgio I, Grygoruk R, dell’Isola F and Steigmann DJ, Pattern formation in the three-dimensional deformations of fibered sheets. *Mech Res Commun.* 69 (2015) 164–171.
- [33] dell’Isola F and Steigmann DJ, A two-dimensional gradient-elasticity theory for woven fabrics, *J. Elasticity* 18 (2015) 113–125.
- [34] Coleman BD, Necking and drawing in polymeric fibers under tension. *Arch. Rational Mech. Anal.* 83 (1983) 115–137.
- [35] Coleman BD and Newman DC, On the Rheology of Cold Drawing: I. Elastic Materials. *J. Polym. Sci. B: Polym. Phys.* 26 (1988) 1801–1822.
- [36] Steigmann DJ and Pipkin AC, Equilibrium of elastic nets. *Phil. Trans. R. Soc. Lond.* 335 (1991) 419–454.
- [37] Ball JM, Currie JC and Olver PJ, Null Lagrangians, weak continuity, and variational problems of arbitrary order. *J. Funct. Anal.* 41 (1981) 135–174.
- [38] Healey TJ and Krömer S, Injective weak solutions in second-gradient nonlinear elasticity. *ESAIM Control Optim. Calc. Var.* 15 (2009) 863–871.
- [39] Turco E and Aristodemo M, A three-dimensional B-spline boundary element. *Comput. Methods Appl. Mech. Eng.* 155 (1998) 119–128.
- [40] Fischer P, Mergheim J and Steinmann P, On the C1 continuous discretization of non-linear gradient elasticity: a comparison of NEM and FEM based on Bernstein-Bézier patches. *Int. J. Numer. Methods Eng.* 82 (2010) 1282–1307.
- [41] Fischer P, Klassen M, Mergheim J, Steinmann P and Müller R, Isogeometric analysis of 2D gradient elasticity. *Comput. Mech.* 47 (2011) 325–334.

- [42] Greco L and Cuomo M, An isogeometric implicit G1 mixed finite element for Kirchhoff space rods. *Comput. Methods Appl. Mech. Eng.* 298 (2016) 325-349.
- [43] Greco L and Cuomo M, An implicit G1 multi patch B-spline interpolation for Kirchhoff–Love space rod. *Comput. Methods Appl. Mech. Eng.* 269 (2014) 17–197.
- [44] Rudrarajua S, Van der Venb A and Garikipati K, Three-dimensional isogeometric solutions to general boundary value problems of Toupin’s gradient elasticity theory at finite strains. *Comput. Methods Appl. Mech. Eng.* 278 (2014) 705–728.
- [45] Cazzani A, Malagù M, Turco E, Isogeometric analysis: a powerful numerical tool for the elastic analysis of historical masonry arches. *Contin. Mech. Thermodyn.* 28 (2016) 139–156.
- [46] Cazzani A, Malagù M, Turco E, Isogeometric analysis of plane-curved beams. *Math. Mech. Solids* (2014) DOI: 10.1177/1081286514531265.
- [47] Cazzani A, Malagù M, Turco E and Stochino F, Constitutive models for strongly curved beams in the frame of isogeometric analysis. *Math. Mech. Solids* 21 (2016) 182–209.
- [48] Luongo A, Mode localization in dynamics and buckling of linear imperfect continuous structures. *Nonlinear Dynam.* 25 (2001) 133–156.
- [49] Luongo A, Zulli D and Piccardo G, On the effect of twist angle on nonlinear galloping of suspended cables. *Comput. & Structures* 87 (2009) 1003–1014.
- [50] Rizzi NL and Varano V, The effects of warping on the postbuckling behaviour of thin-walled structures. *Thin-Wall. Struct.* 49 (2011) 1091–1097.
- [51] Gabriele S, Rizzi NL and Varano V, On the imperfection sensitivity of thin-walled frames. *Civil-Comp Proceedings* 99 (2012).
- [52] Rizzi NL, Varano V and Gabriele S, Initial postbuckling behavior of thin-walled frames under mode interaction. *Thin-Wall. Struct.* 68 (2013) 124–134.